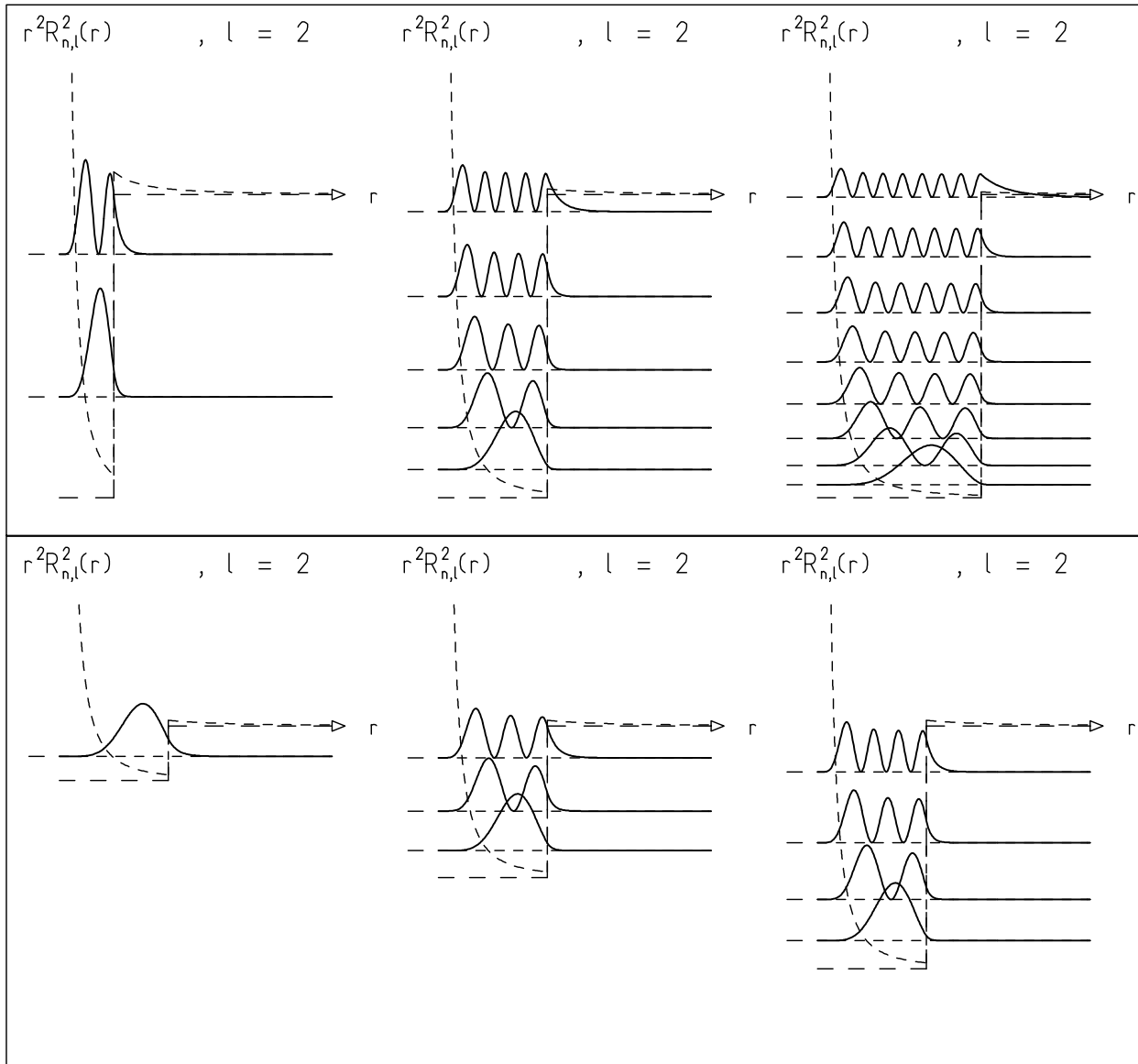


**Fig. 13.1.** The radial eigenfunctions  $R_{n\ell}(r)$  of bound states in a square-well potential for three angular-momentum values,  $\ell = 0, 1, 2$ , are shown as continuous lines in the left column. The form  $V(r)$  of the potential is indicated by the long-dash line. Also shown for  $\ell \neq 0$  is the effective potential  $V_\ell^{\text{eff}}(r)$  which contains the influence of angular momentum. On the left is an energy scale and to the right of it the energy eigenvalues  $E_n$  are indicated by horizontal lines. These lines are repeated as short-dash lines on the right. They serve as zero lines for the plotted functions. In the middle column the squares  $R_{n\ell}^2(r)$  of the radial eigenfunctions are shown. Along a fixed direction  $\vartheta, \phi$  away from the origin, this quantity is proportional to the probability that the particle will be observed within a unit volume element around point  $r, \vartheta, \phi$ . In the right column are the functions  $r^2 R_{n\ell}^2(r)$ . Their values are a measure for the probability of observing the particle anywhere within a spherical shell of radius  $r$  and unit thickness.



**Fig. 13.2.** Dependence of the eigenvalue spectrum of a square-well potential on (top) the width and (bottom) the depth of the well. The function shown is  $r^2 R_{n\ell}^2(r)$  for the fixed angular-momentum quantum number  $\ell = 2$ .

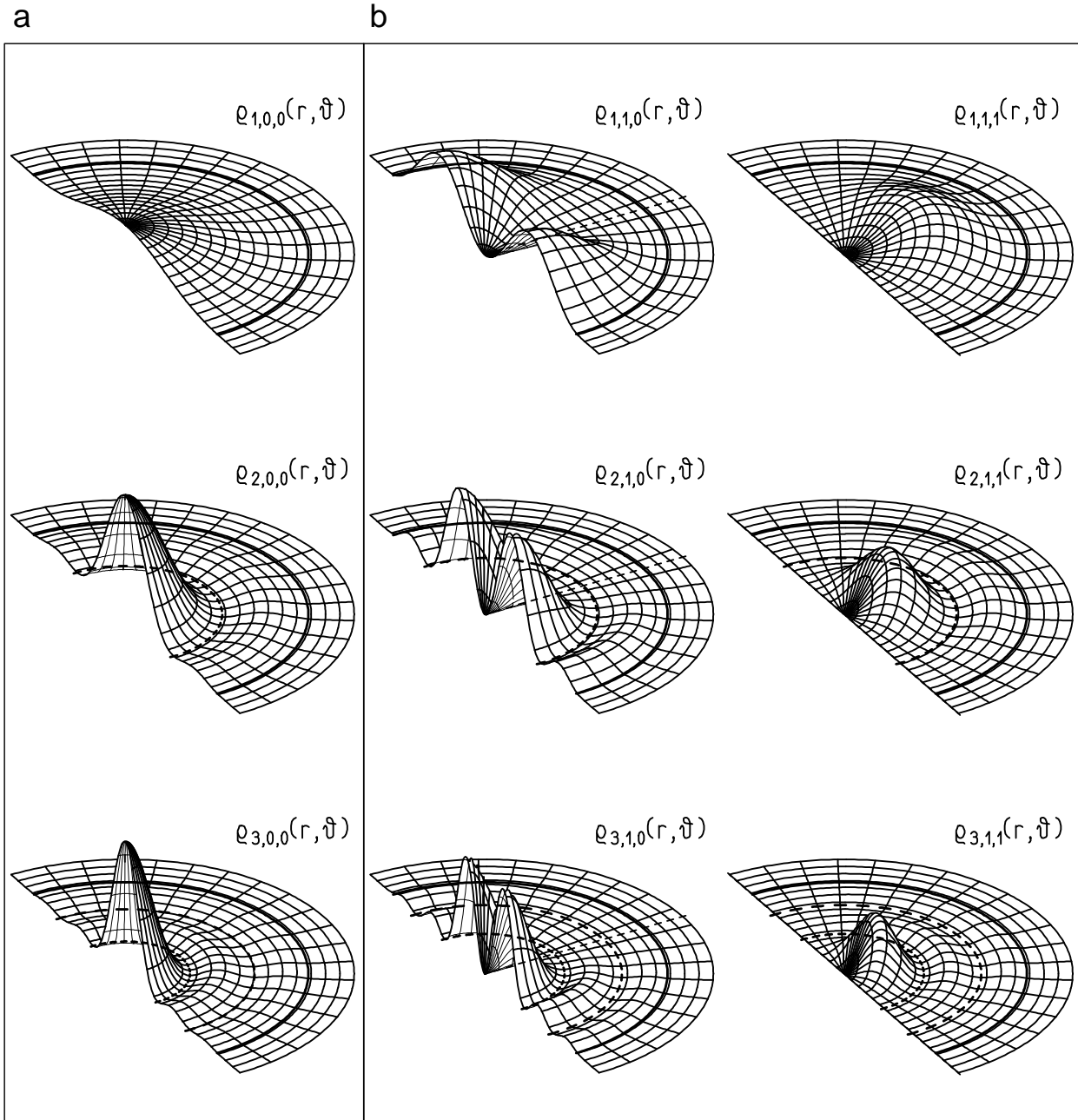
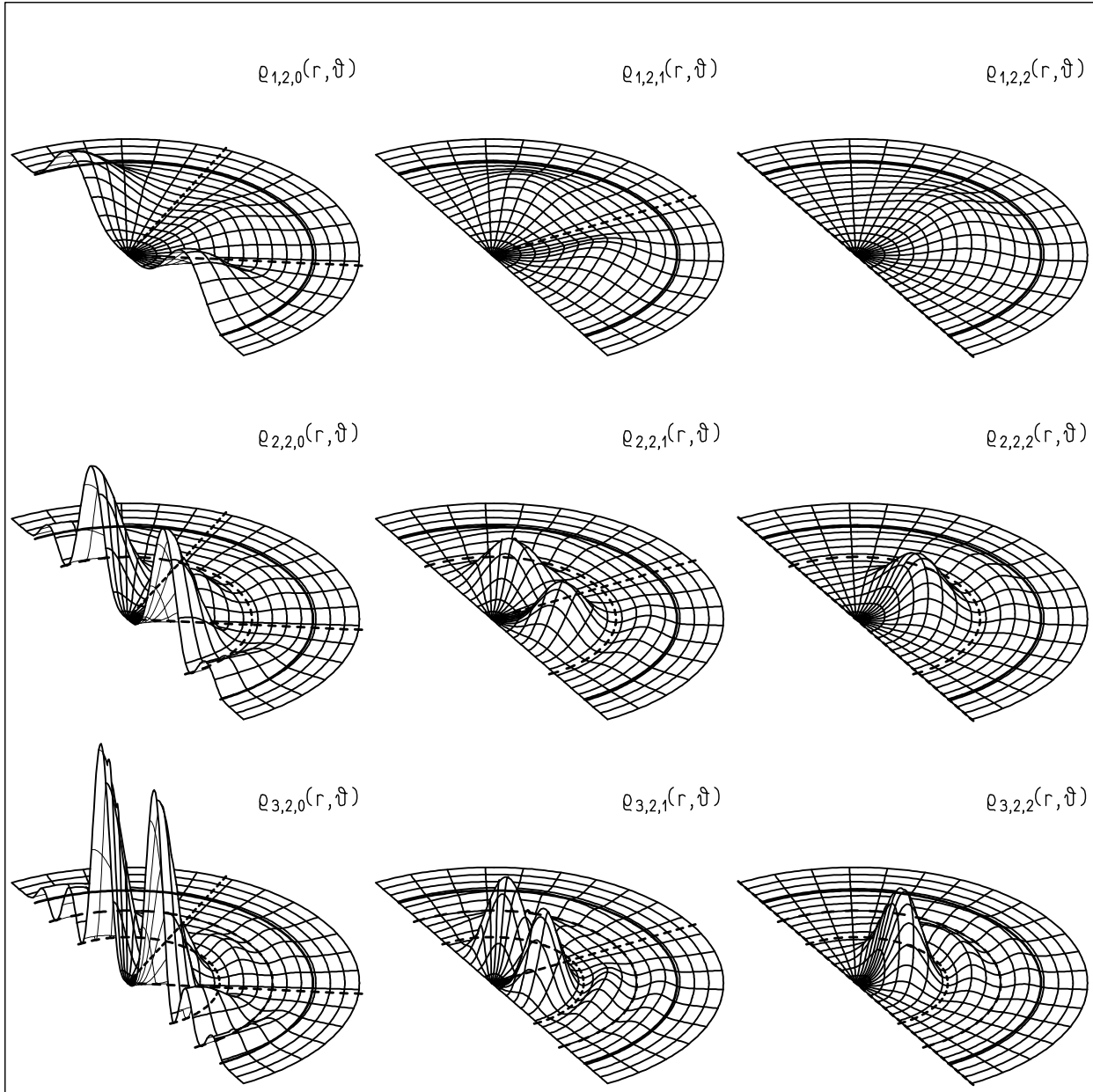
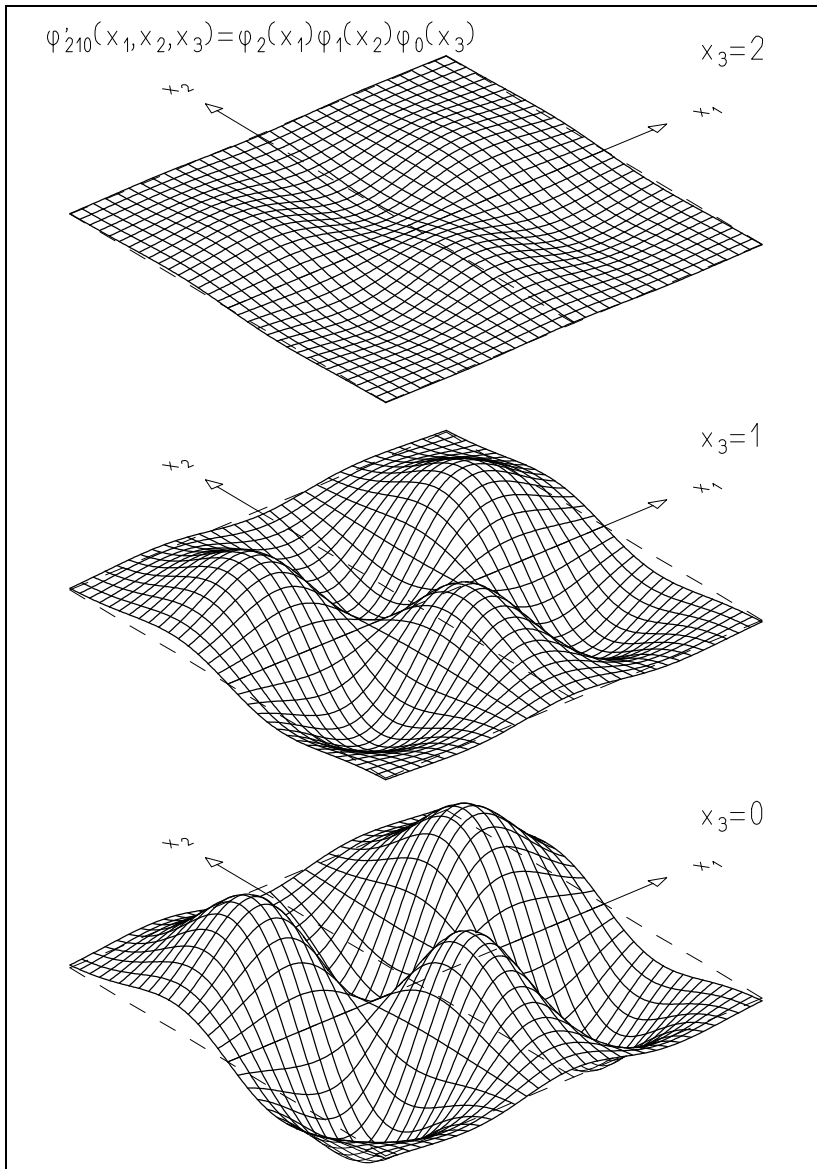


Fig. 13.3. Absolute squares  $\rho_{n\ell m}(r, \vartheta) = |\varphi_{n\ell m}(r, \vartheta, \phi)|^2$  of the full three-dimensional eigenfunction of a square-well potential. Here  $\rho_{n\ell m}(r, \vartheta)dV$  represents the probability of observing the particle in the volume element  $dV$  at location  $(r, \vartheta, \phi)$ . It is a function only of the distance  $r$  from the origin and of the polar angle  $\vartheta$ . (a) In this figure, which applies to zero angular-momentum quantum number  $\ell$ , the function  $\varphi(r)$  depends only on  $r$ . For values  $n = 1, 2, 3$  of the principal quantum number it has  $n - 1 = 0, 1, 2$  nodes in  $r$  indicated by the dashed half-circles. Each plot gives the probability density for observing the particle at any point in a half-plane containing the  $z$  axis. Here and in Figure 13.4 all plots have the same scale in  $r$  and  $\vartheta$ . They do, however, have different scale factors in  $\rho$ . (b) The functions  $\rho_{n\ell m}(r, \vartheta)$  as given in (a) but for  $\ell = 1$  and  $m = 0, 1$ . The  $\vartheta$  dependence is given by the Legendre functions  $P_\ell^{|m|}(\cos \vartheta)$  which have  $\ell - |m|$  nodes in  $\vartheta$ , indicated by the dashed lines  $\vartheta = \text{const.}$



**Fig. 13.4.** The functions  $\rho_{n\ell m}(r, \vartheta)$  as given in Figure 13.3 but for  $\ell = 2$  and  $m = 0, 1, 2$ .





**Fig. 13.5. Eigenfunction  $\varphi'_{210}(x_1, x_2, x_3) = \varphi_2(x_1)\varphi_1(x_2)\varphi_0(x_3)$  of the three-dimensional harmonic oscillator expressed in Cartesian coordinates  $x_1, x_2, x_3$  and written as a product of three one-dimensional harmonic-oscillator eigenfunctions. For this figure the width parameter  $\sigma_0 = 1$  was chosen. The function is plotted for three planes  $x_3 = 0, 1, 2$ . Because  $\varphi_0(x_3)$  is symmetric, the plots remain unchanged if the substitution  $x_3 \rightarrow -x_3$  is performed. This figure should be compared with Figure 6.4.**

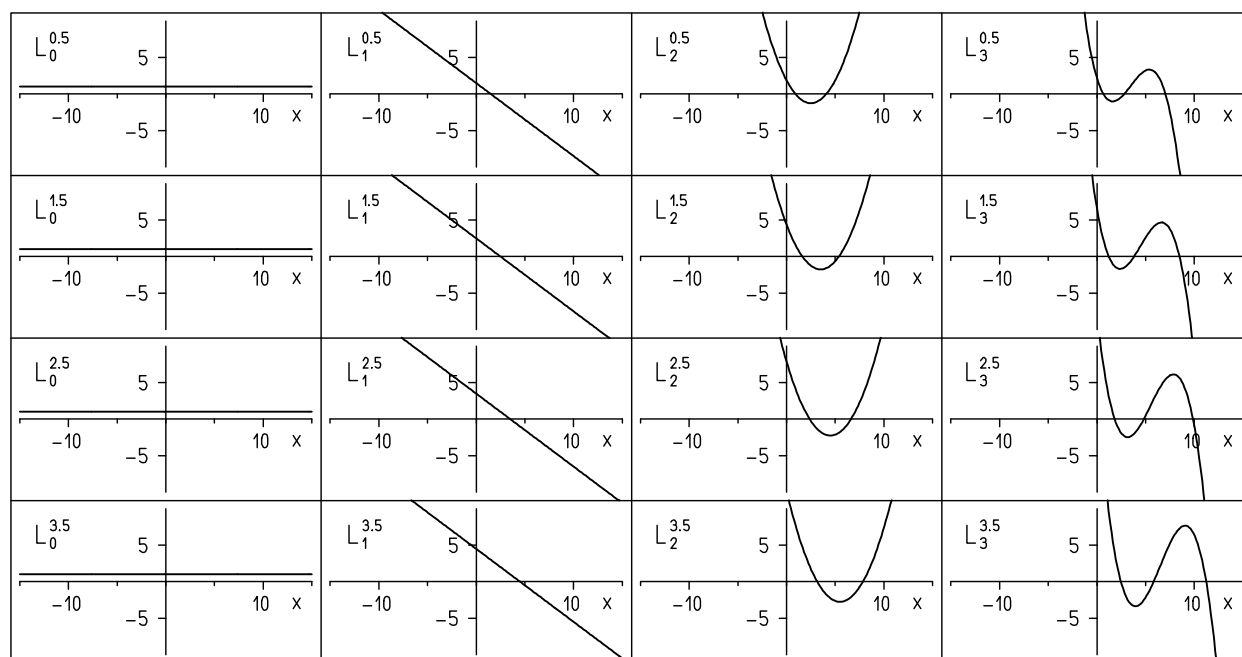


**Fig. 13.6.** Laguerre polynomials of half-integer upper index. The lower index is equal to the degree of the polynomial and to the number of its zeros. All zeros are at positive values of the argument  $x$ .

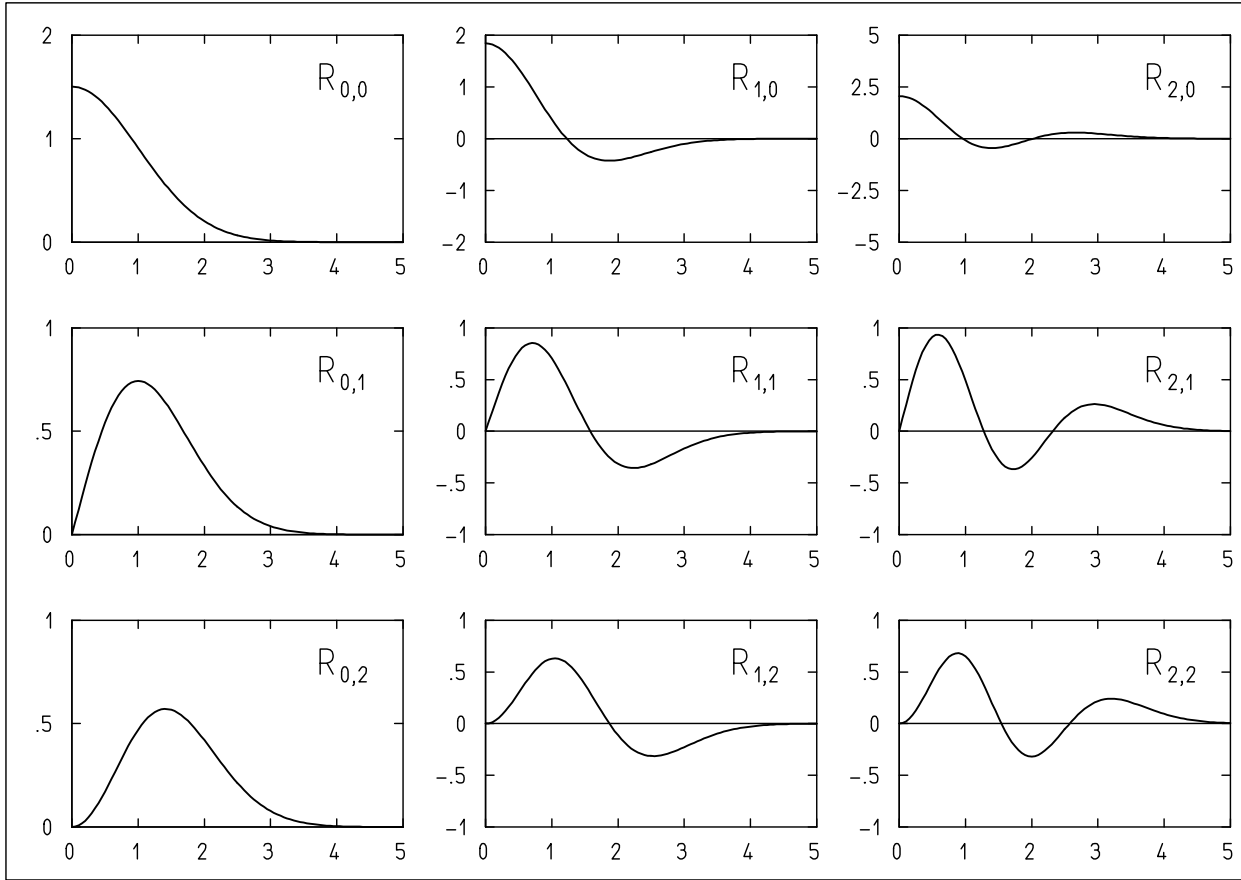


**Fig. 13.7.** Radial eigenfunctions  $R_{n,\ell}(\rho)$ ,  $n = 2n_r + \ell$  for the three-dimensional harmonic oscillator. Their zeros are the  $(n-1)/2$  zeros of the Laguerre polynomial  $L_{(n-\ell)/2}^{\ell+1/2}(\rho^2)$ . The argument  $\rho$  is the distance  $r$  from the origin divided by the width  $\sigma_0$  of the ground state of the oscillator. Graphs in the same column belong to the same value of  $n_r$ . Graphs in the same row belong to the same value of  $\ell$ .

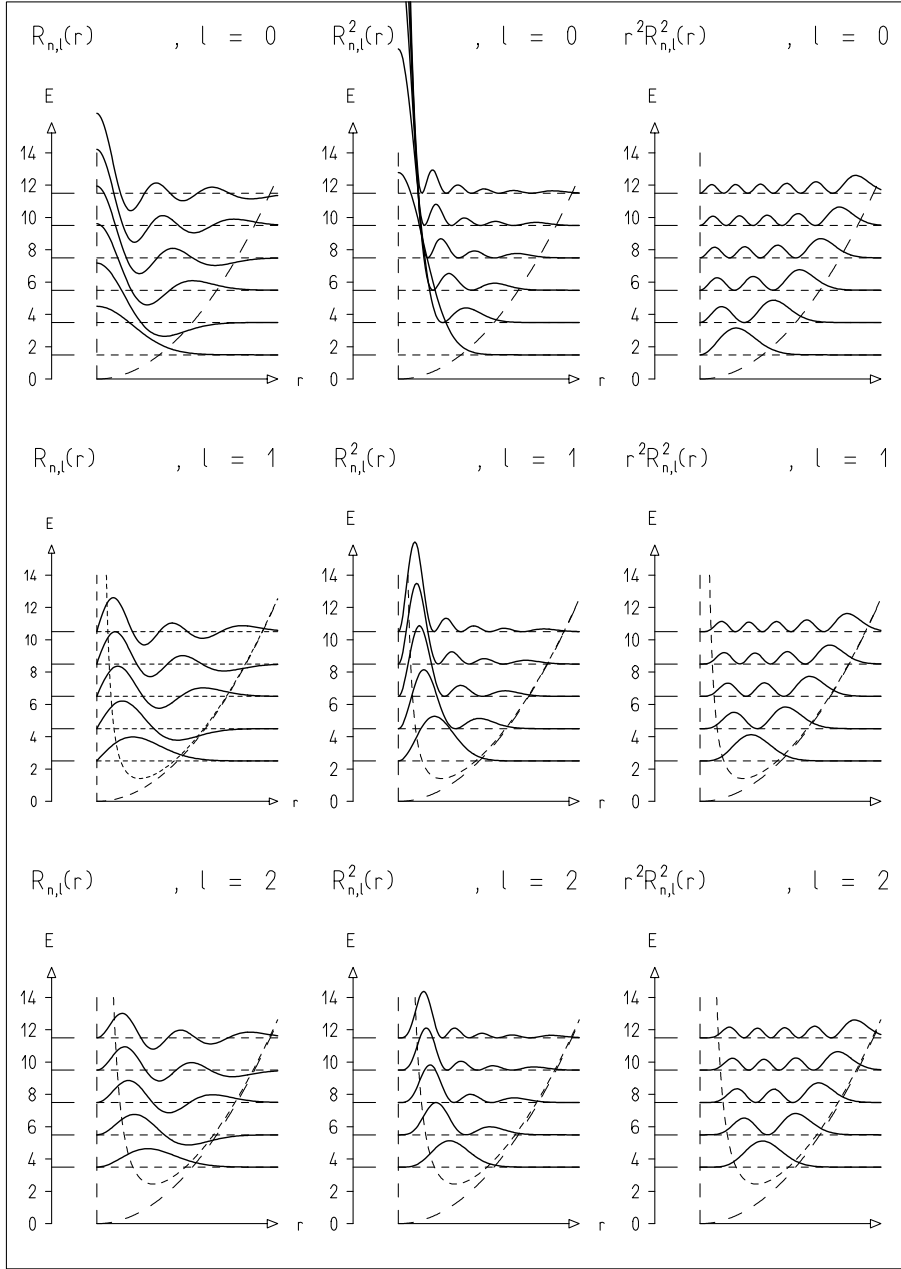


**Fig. 13.8.** Radial eigenfunctions  $R_{n\ell}(r)$ , their squares  $R_{n\ell}^2(r)$ , and the functions  $r^2 R_{n\ell}^2(r)$  for the lowest eigenstates of the harmonic oscillator and the lowest angular-momentum quantum numbers  $\ell = 0, 1, 2$ . On the left side are the eigenvalue spectra. The form of the harmonic-oscillator potential  $V(r)$  is indicated by a long-dash line, and, for  $\ell \neq 0$ , that of the effective potential  $V_{\ell}^{\text{eff}}(r)$  by a short-dash line. The eigenvalues have equidistant spacing. The eigenvalue spectra are degenerate for all even  $\ell$  values and all odd  $\ell$  values, except that the minimum value of the principal quantum number is  $n = \ell$ .

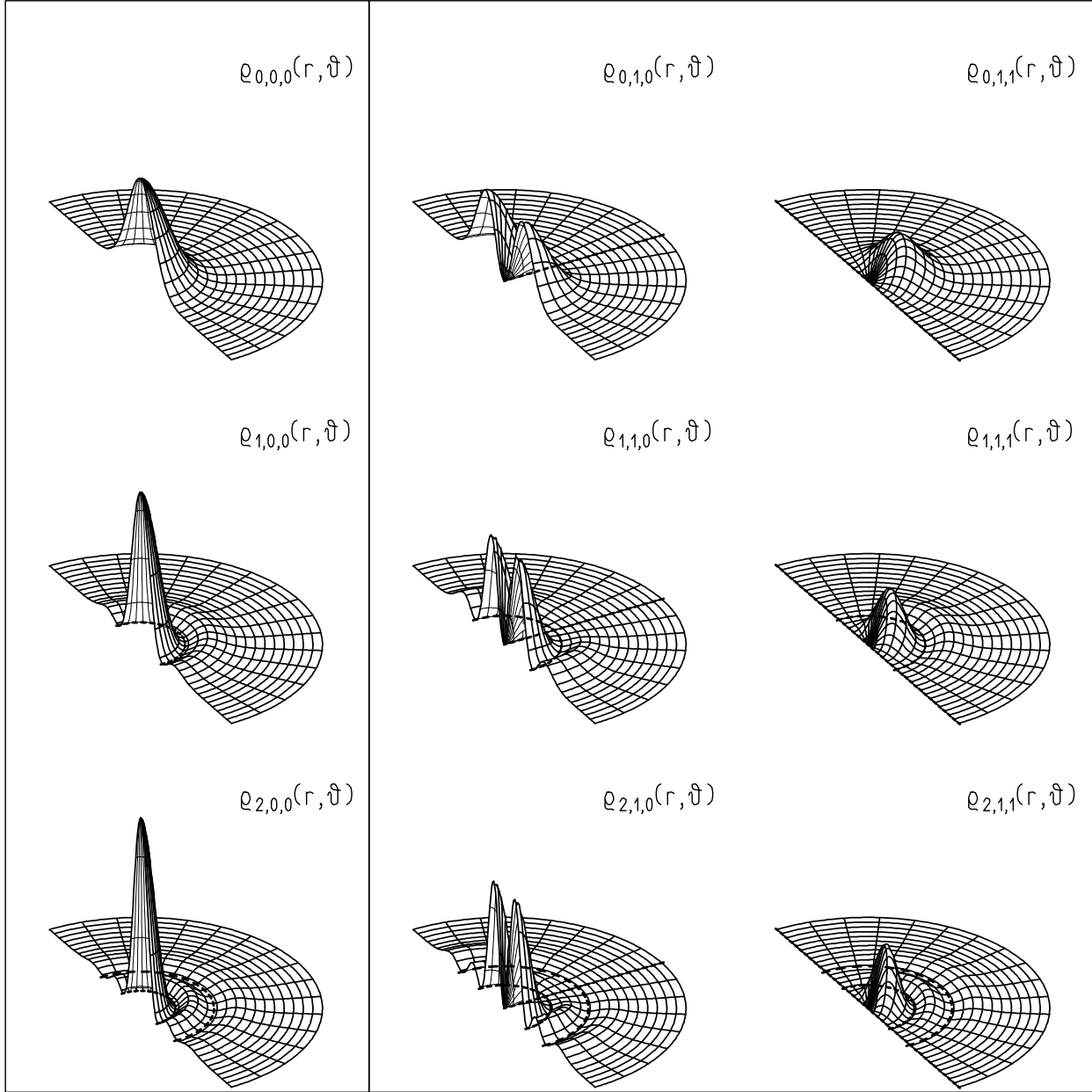


**Fig. 13.9.** The absolute squares  $\rho_{n_r \ell m}(r, \vartheta) = |\varphi_{n_r \ell m}(r, \vartheta, \phi)|^2$ ,  $n_r = (n - \ell)/2$  of the full three-dimensional eigenfunctions for the harmonic oscillator. The absolute squares are functions only of  $r$  and  $\vartheta$ . There are  $n_r$  radial nodes, and  $\ell - |m|$  polar nodes, indicated by dashed half-circles and rays, respectively. Each figure gives the probability density for observing the particle at any point in a half-plane containing the  $z$  axis. All pictures have the same scale in  $r$  and  $\vartheta$ . They do, however, have different scale factors in  $\rho$ . In this figure the  $\rho_{n_r \ell m}$  are shown for  $\ell = 0$  (left) and  $\ell = 1$  (right).

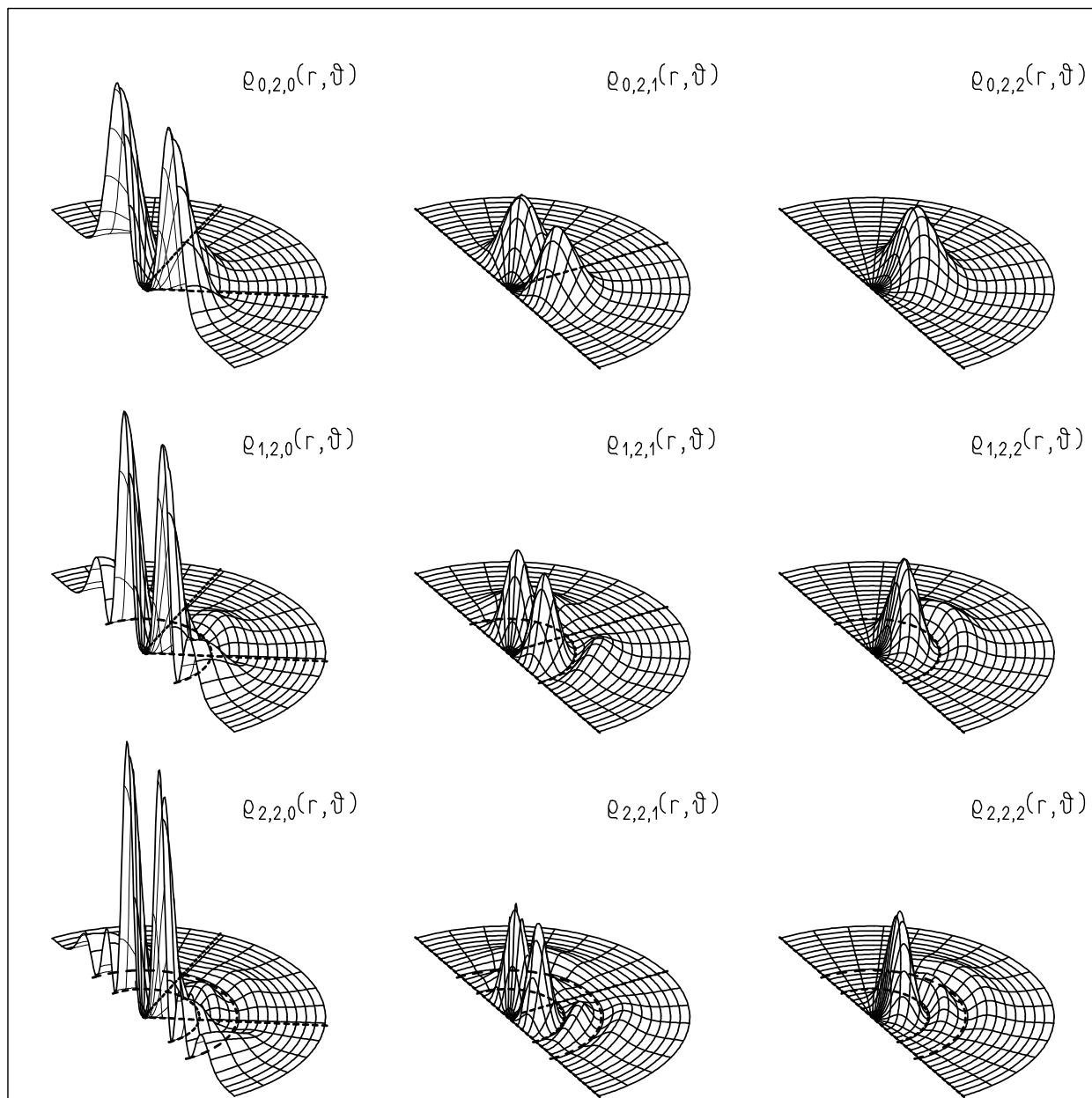
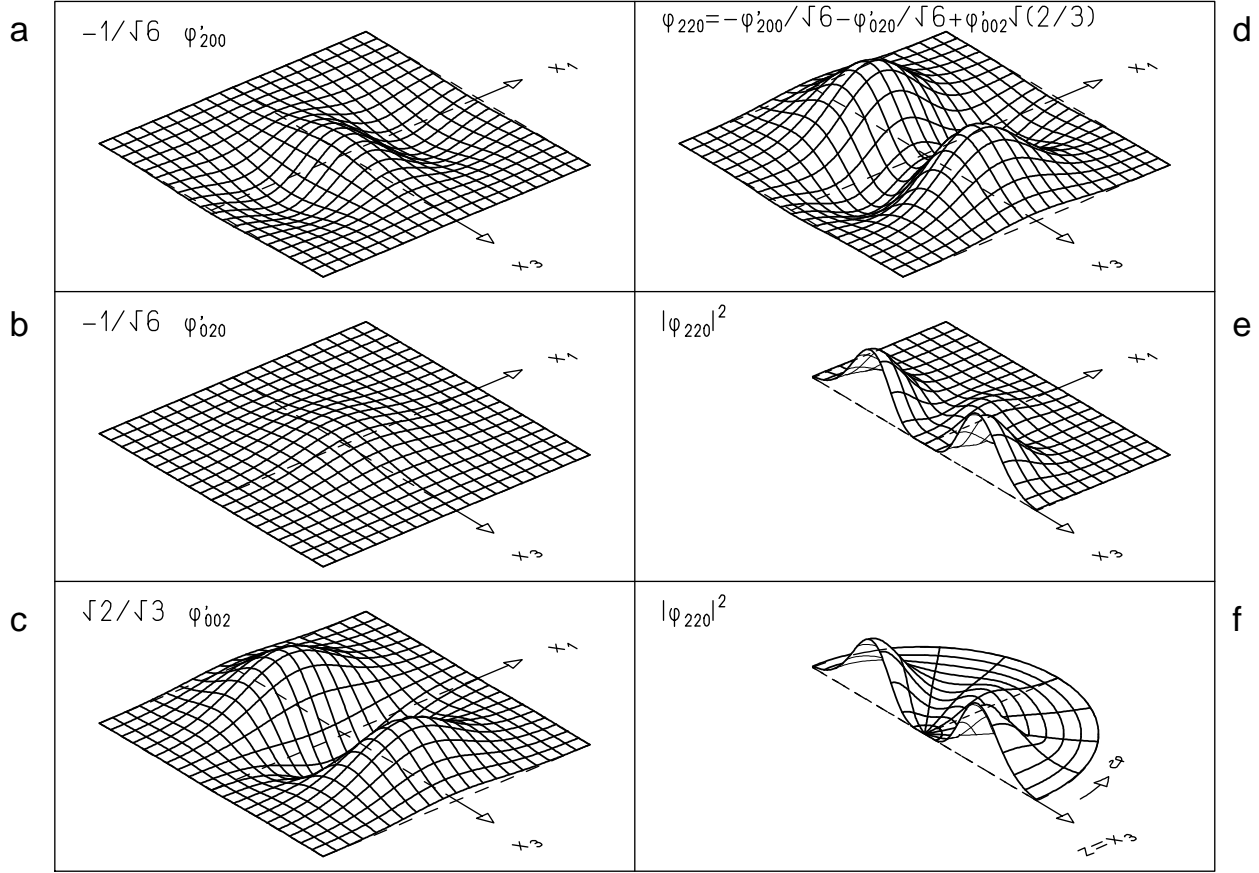
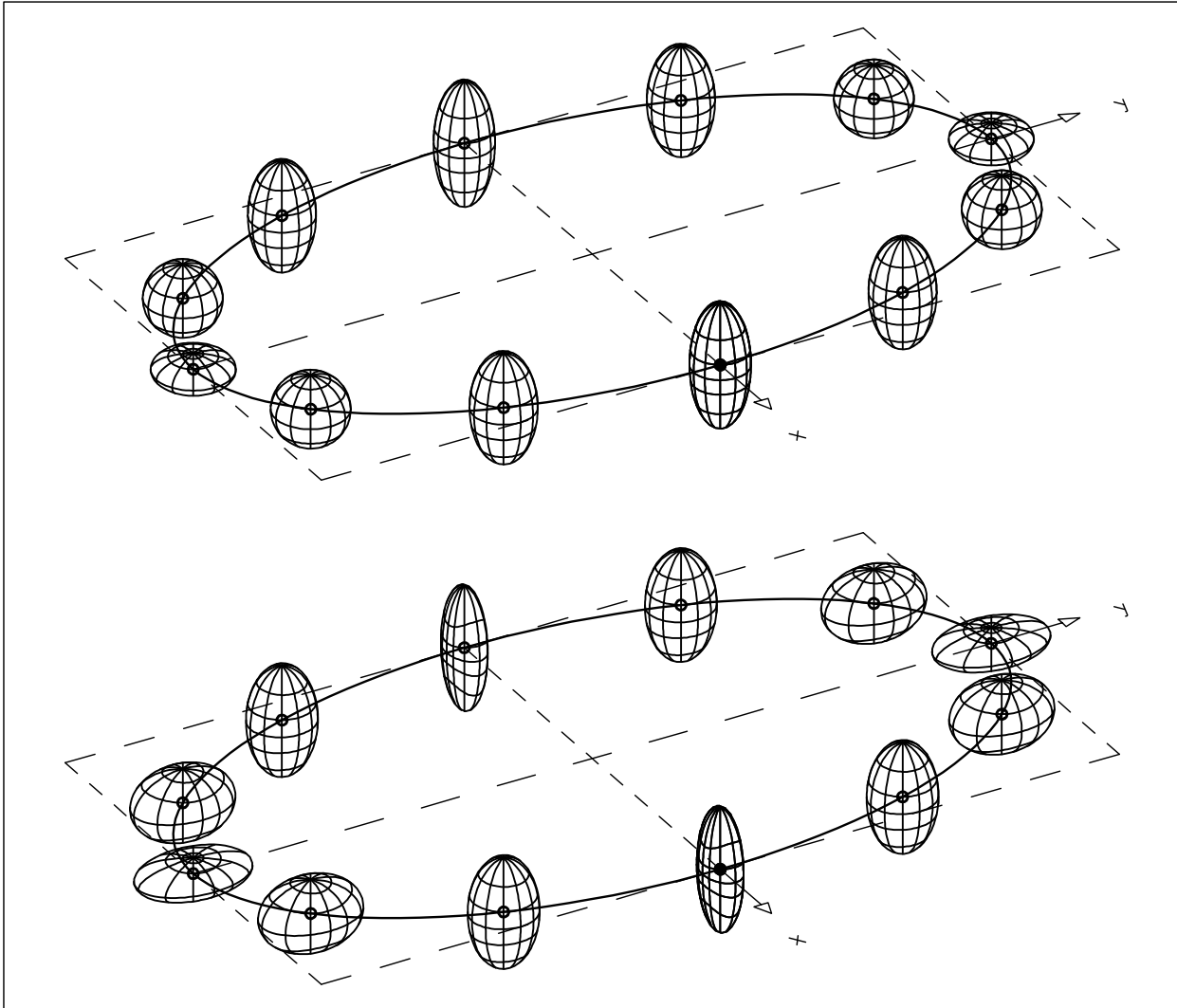


Fig. 13.10. As Figure 13.9 but for  $l = 2$ .



**Fig. 13.11.** An eigenstate  $\varphi_{nlm}(r, \vartheta, \phi)$  of the harmonic oscillator can be written as a linear superposition of the degenerate eigenfunctions  $\varphi'_{n_1 n_2 n_3}(x_1, x_2, x_3)$  having the same energy eigenvalue  $(\vec{a}, \vec{b}, \vec{c})$ . The three eigenfunctions for  $n = 2$  in the  $x_1, x_2$  plane each multiplied by the appropriate factor; (d) the sum; (e) its square; (f) the function  $|\varphi_{220}|^2$  in  $r, \vartheta$  representation as known from Figure 13.10. Parts e and f are identical except that part e has Cartesian coordinates, part f polar coordinates.



**Fig. 13.12.** A three-dimensional Gaussian wave packet, represented by its probability ellipsoid, moves under the influence of an attractive force described by a harmonic-oscillator potential. Its expectation value, that is, the center of the ellipsoid, describes an elliptical trajectory. The initial conditions were chosen so that the ellipsoid does not tumble, that is, its principal axes keep constant orientations. The magnitudes of the principal axes oscillate with twice the oscillator frequency. Two examples are shown. Top: The ellipsoid stays rotationally symmetric with respect to the  $z$  axis. Bottom: All three principal axes of the ellipsoid are different.



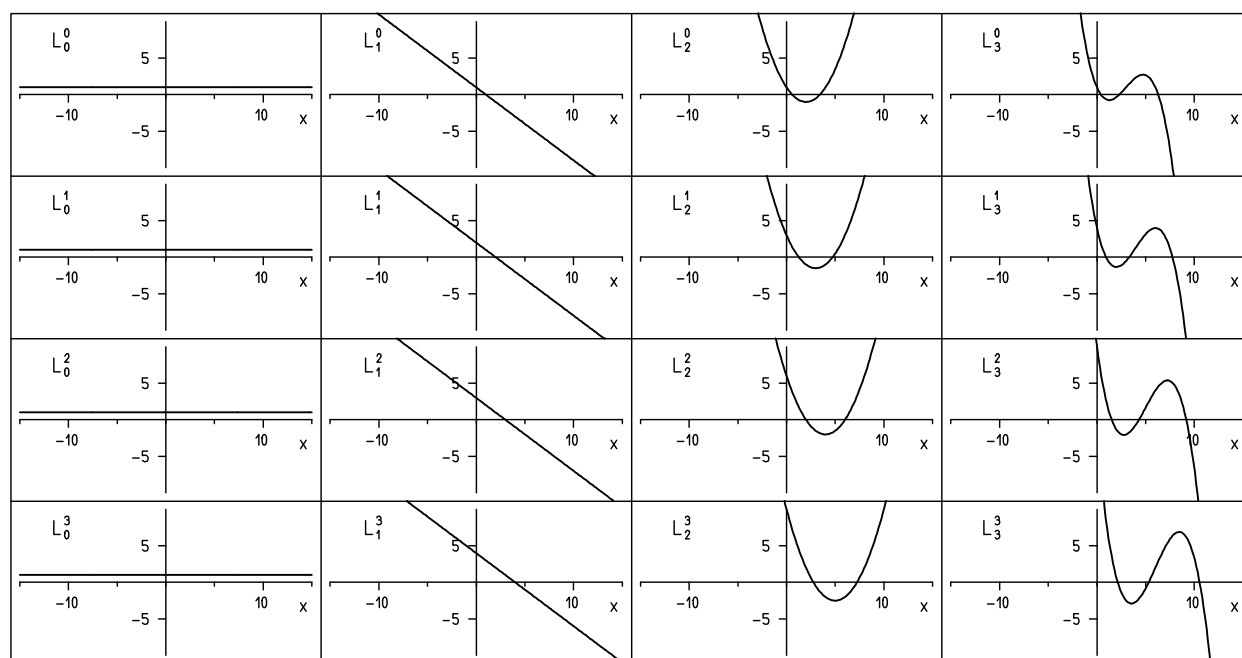


**Fig. 13.13.** Laguerre polynomials of integer upper index. The lower index is equal to the degree of the polynomial and to the number of its zeros. All zeros are at positive values of the argument  $x$ . The graphs look rather similar to those of Figure 13.6, which shows the Laguerre polynomials of half-integer upper index. That they are in fact different can be seen, for example, from the positions of the zeros.

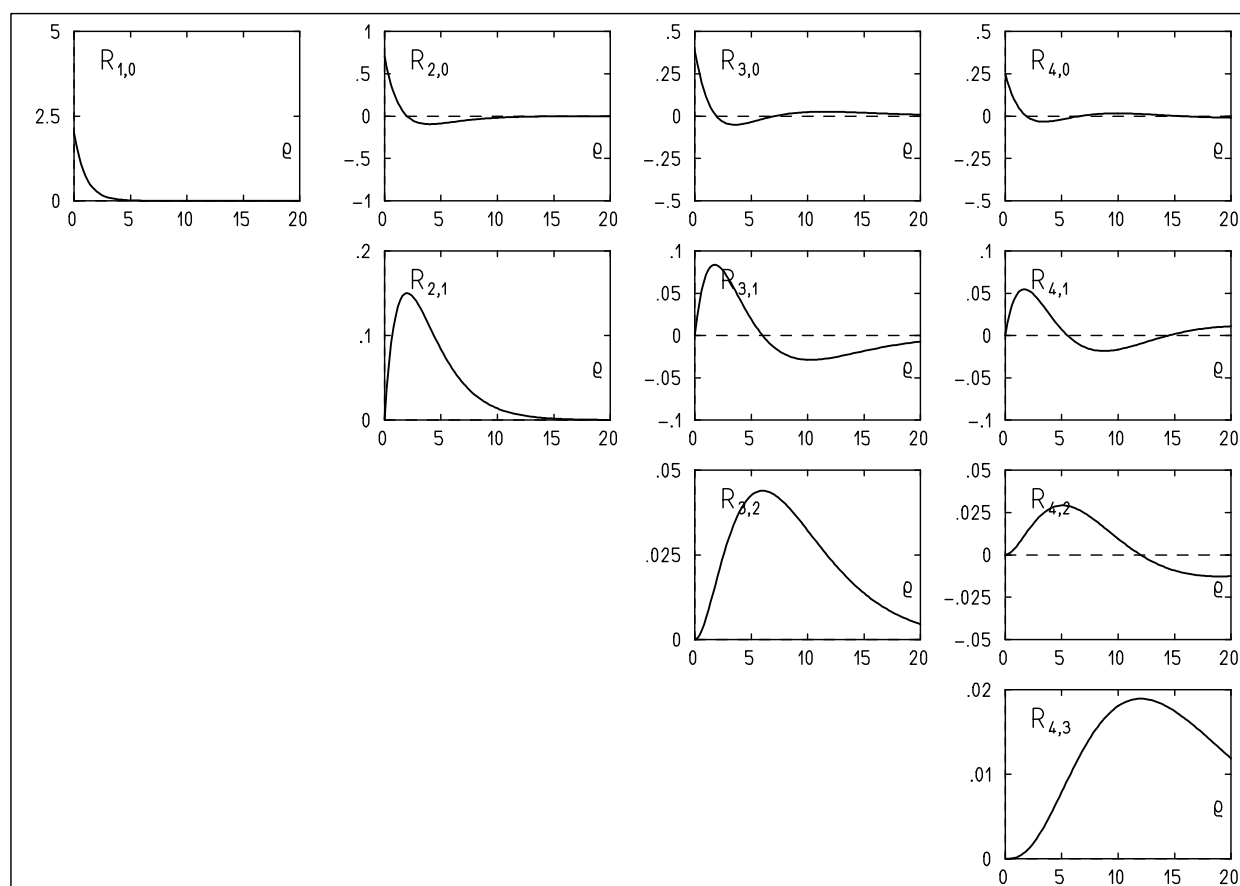


**Fig. 13.14.** Radial eigenfunctions  $R_{n\ell}(\rho)$  for the electron in the hydrogen atom. Their zeros are the  $n - \ell - 1$  zeros of the Laguerre polynomials  $L_{n-\ell-1}^{2\ell+1}(2\rho/n)$ . Here the argument of the Laguerre polynomial is  $2\rho/n$  with  $n$  being the principal quantum number and  $\rho = r/a$  the distance between electron and nucleus divided by the Bohr radius  $a$ .

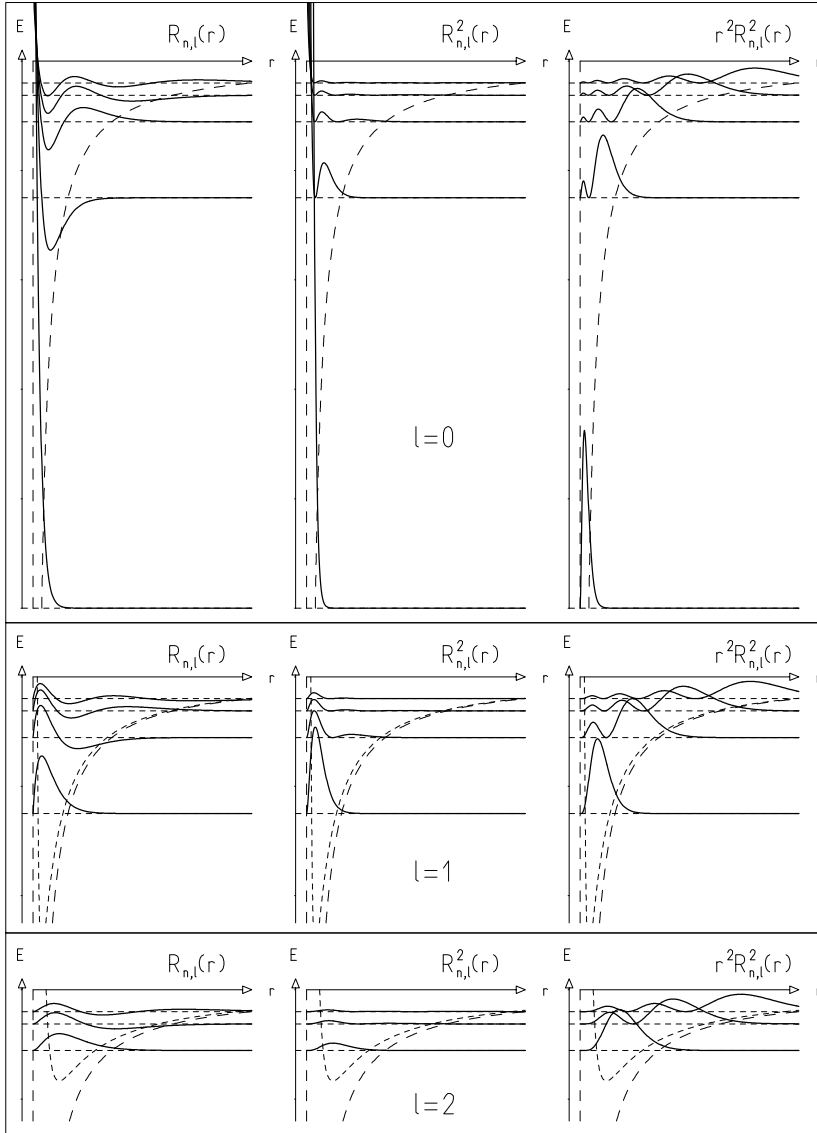


**Fig. 13.15.** Radial eigenfunctions  $R_{n\ell}(r)$ , their squares  $R_{n\ell}^2(r)$ , and the functions  $r^2 R_{n\ell}^2(r)$  for the lowest eigenstates of the electron in the hydrogen atom and the lowest angular-momentum quantum numbers  $\ell = 0, 1, 2$ . Also shown are the energy eigenvalues as horizontal dashed lines, the form of the Coulomb potential  $V(r)$ , and, for  $\ell \neq 0$ , the forms of the effective potential  $V_\ell^{\text{eff}}(r)$ . The eigenvalue spectra are degenerate for all  $\ell$  values, except that the minimum value of the principal quantum number is  $n = \ell + 1$ .

$$\rho_{nlm}(r, \vartheta) = |\varphi_{nlm}(r, \vartheta, \phi)|^2$$

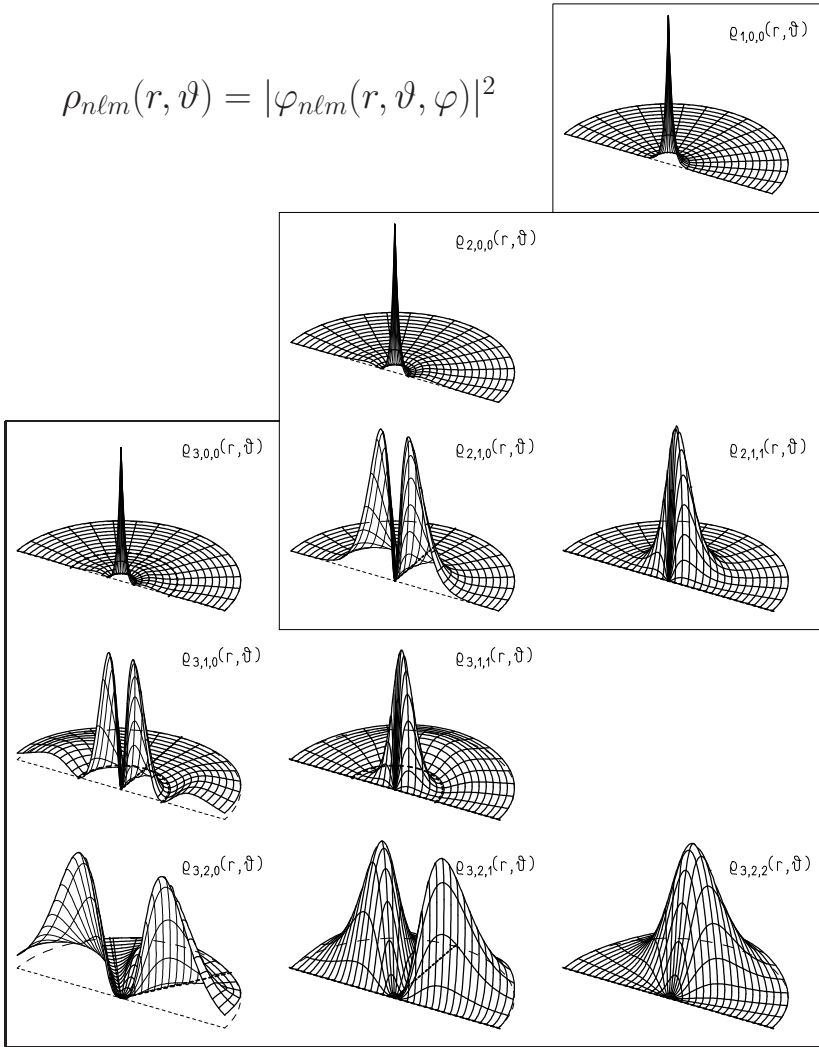


**Fig. 13.16.** The absolute squares  $\rho_{nlm}(r, \vartheta) = |\varphi_{nlm}(r, \vartheta, \phi)|^2$  of the full three-dimensional wave functions for the electron in the hydrogen atom. They are functions only of  $r$  and  $\vartheta$ . All eigenstates having the same principal quantum number have the same energy eigenvalue  $E_n$ . The possible angular-momentum quantum numbers are  $\ell = 0, 1, \dots, n-1$ . The wave functions have  $n - \ell - 1$  nodes in  $r$  and  $\ell - |m|$  nodes in  $\vartheta$ , indicated by dashed half-circles and rays, respectively. Each figure gives the probability density for observing the electron at any point in a half-plane containing the  $z$  axis. All pictures have the same scale in  $r$  and  $\vartheta$ . They do, however, have different scale factors in  $\rho$ .

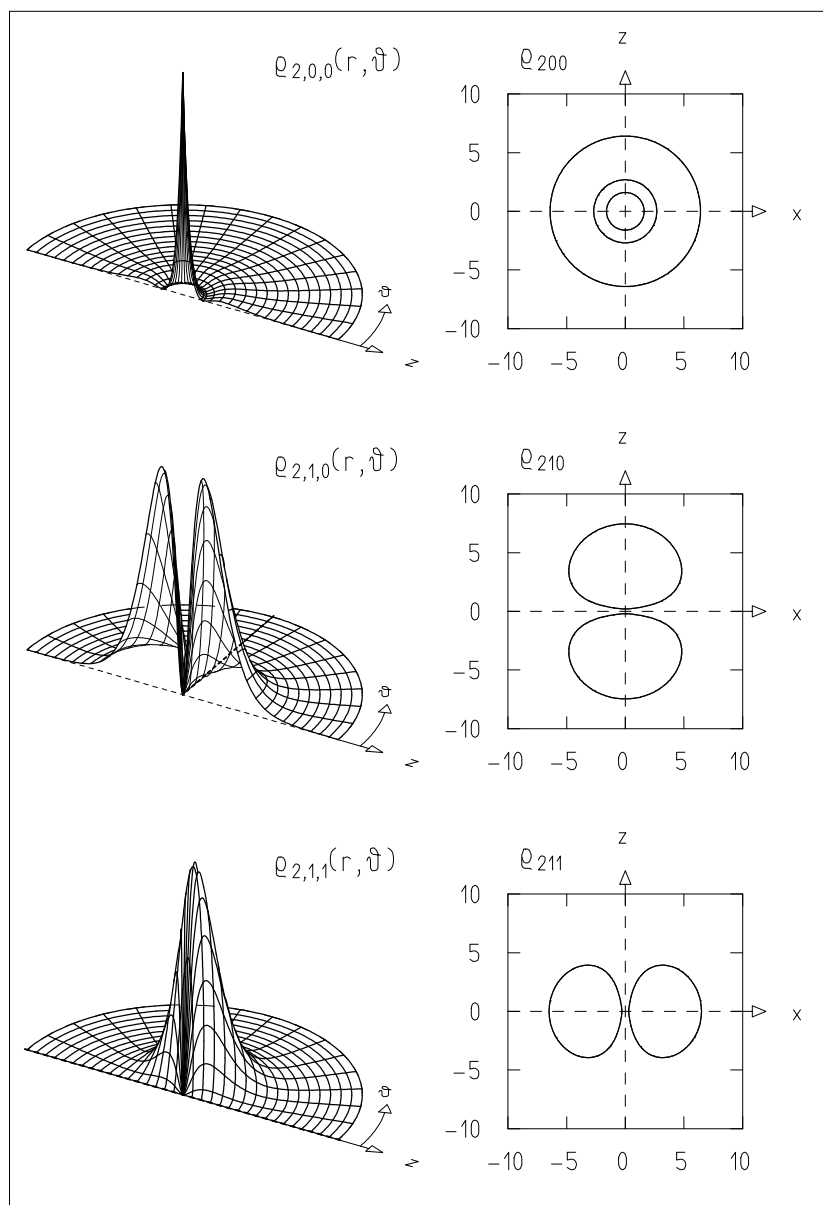


**Fig. 13.17.** Left: Spatial probability density  $\rho_{2\ell m}$  for an electron in the hydrogen atom shown over a half-plane bounded by the  $z$  axis. Different scales in  $\rho_{2\ell m}$  are used in the three plots. Right: Contour lines  $\rho_{2\ell m} = 0.002$  in the  $x, z$  plane. Numbers are in units of the Bohr radius.

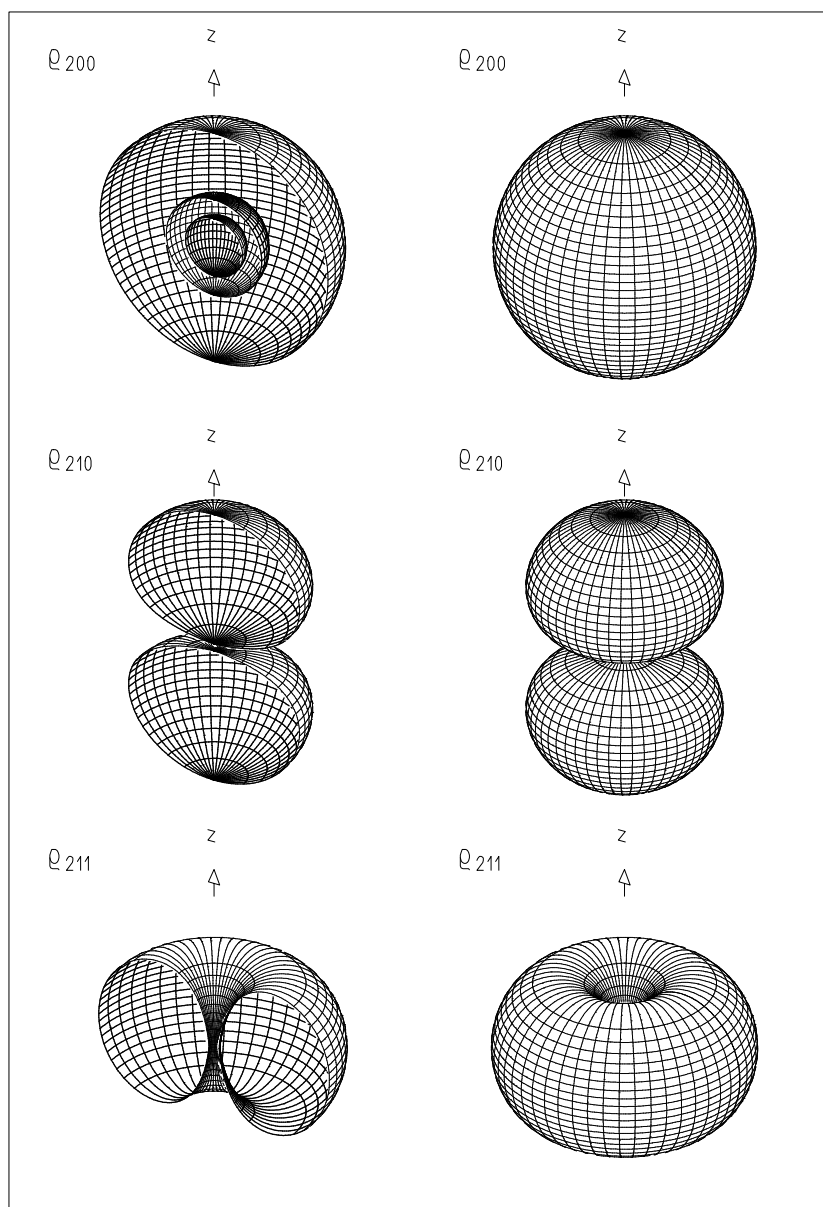


**Fig. 13.18.** Surfaces of constant probability density  $\rho_{2\ell m} = 0.002$  in full  $x, y, z$  space (right) and in the half-space  $x > 0$  (left).

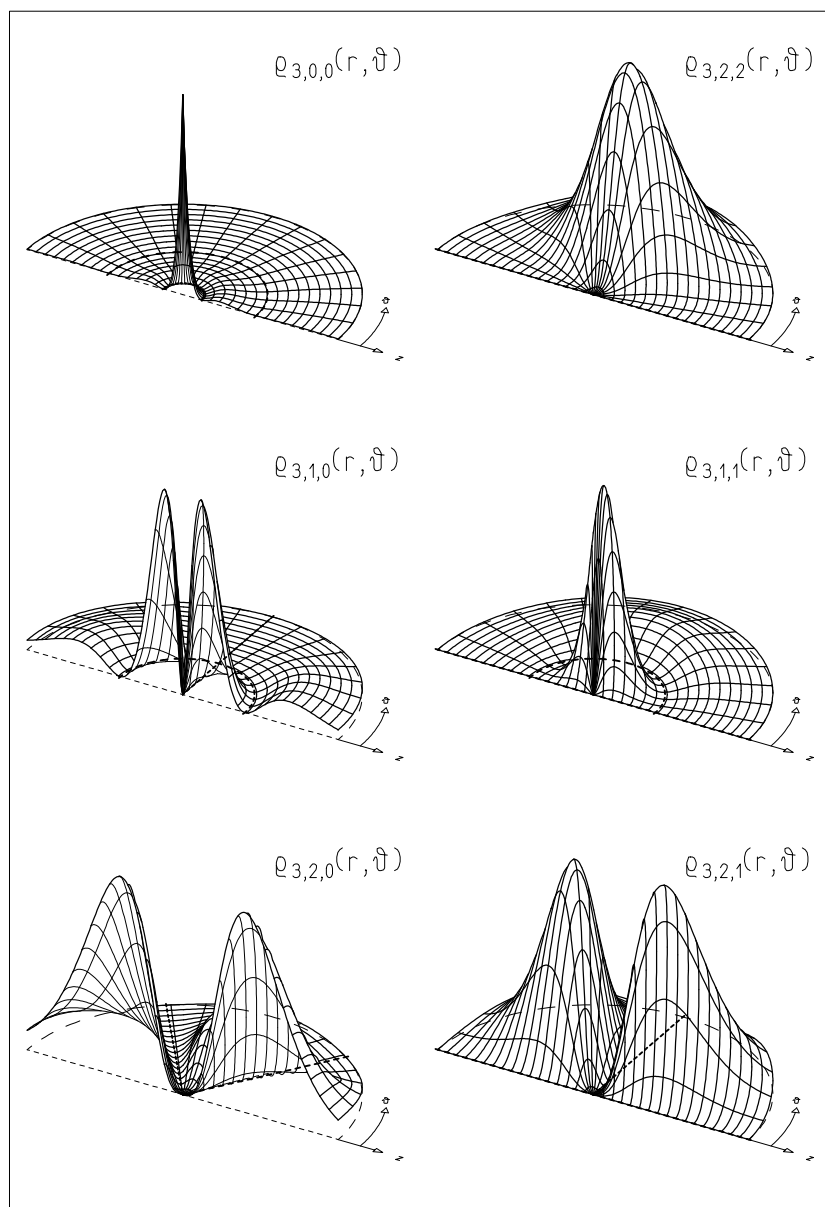


**Fig. 13.19.** Spatial probability density  $\rho_{3\ell m}$  for an electron in the hydrogen atom shown over a half-plane bounded by the  $z$  axis. Different scales in  $\rho_{3\ell m}$  are used.

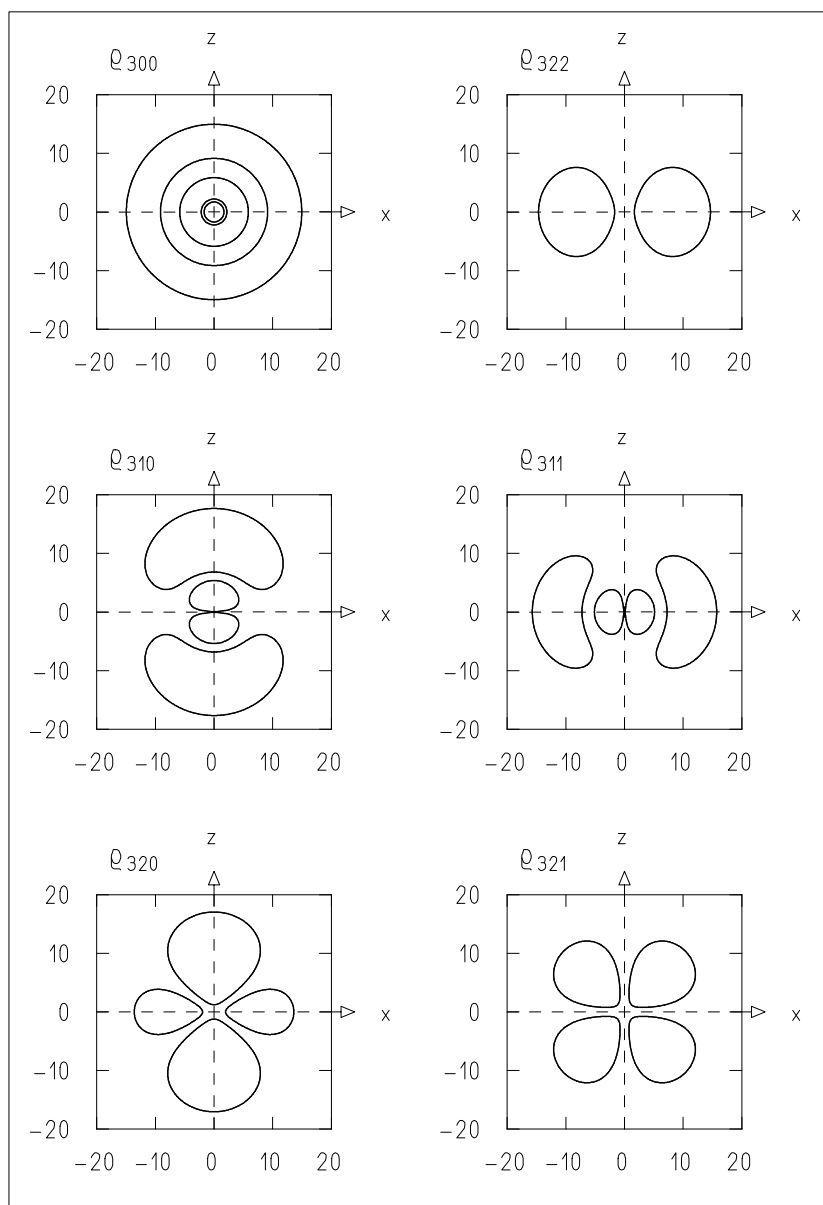


**Fig. 13.20.** Contour lines  $\rho_{3\ell m} = 0.0002$  in the  $x, z$  plane. Numbers are in units of the Bohr radius.



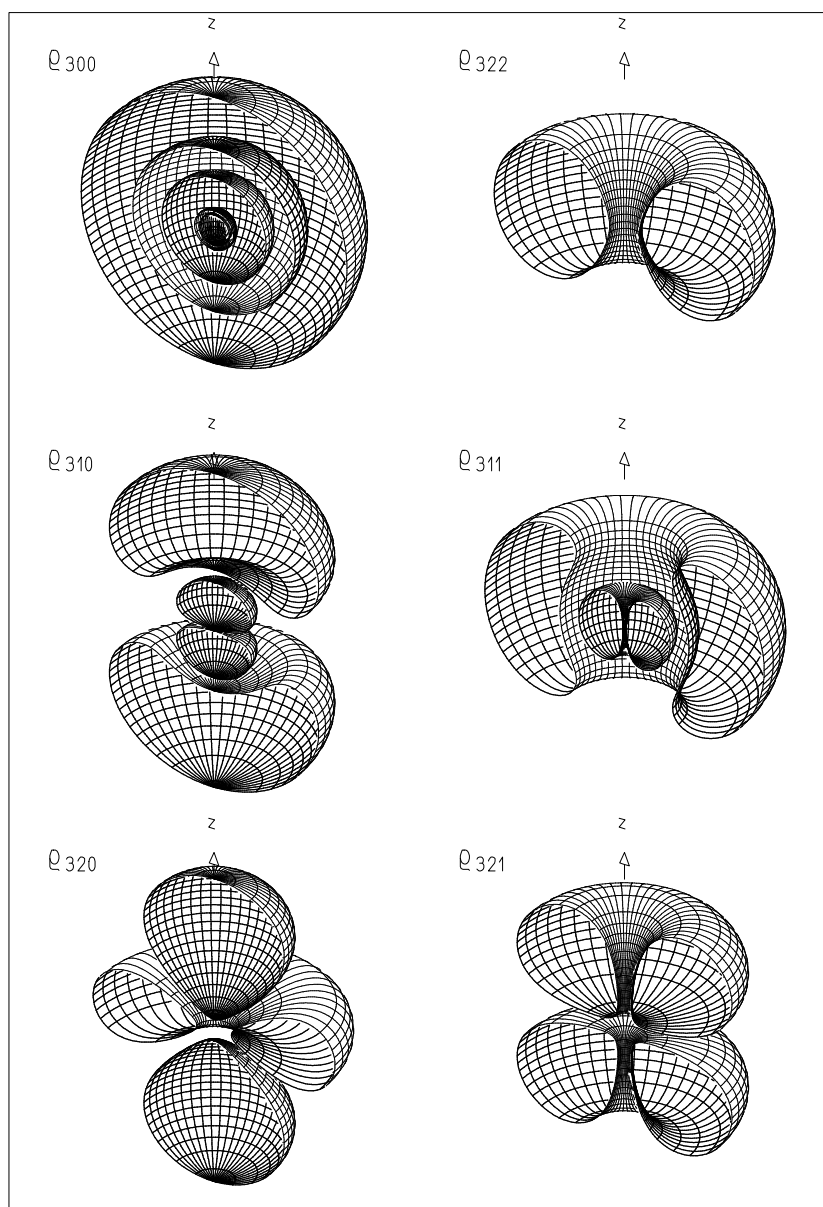


**Fig. 13.21.** Surfaces of constant probability density  $\rho_{3\ell m} = 0.0002$  in the half-space  $x > 0$ .

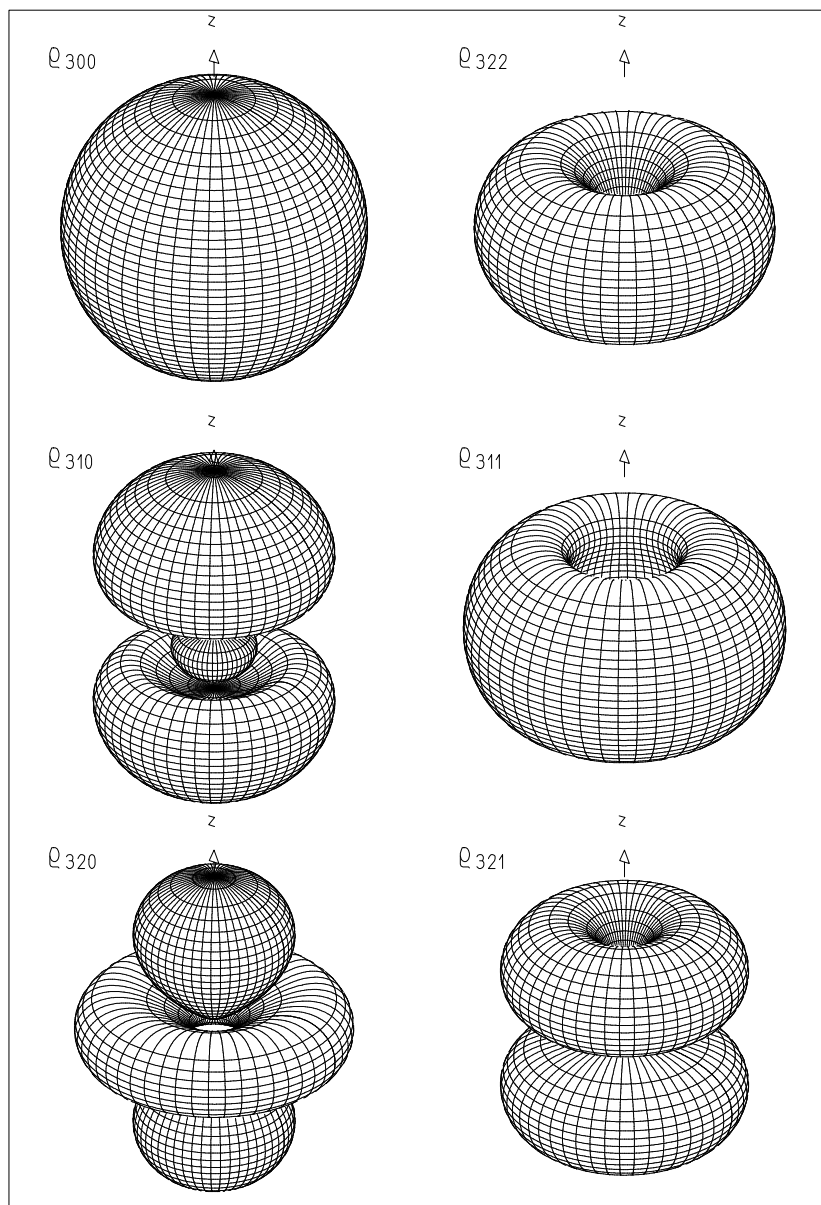


**Fig. 13.22.** Surfaces of constant probability density  $\rho_{3\ell m} = 0.0002$  in full  $x, y, z$  space.

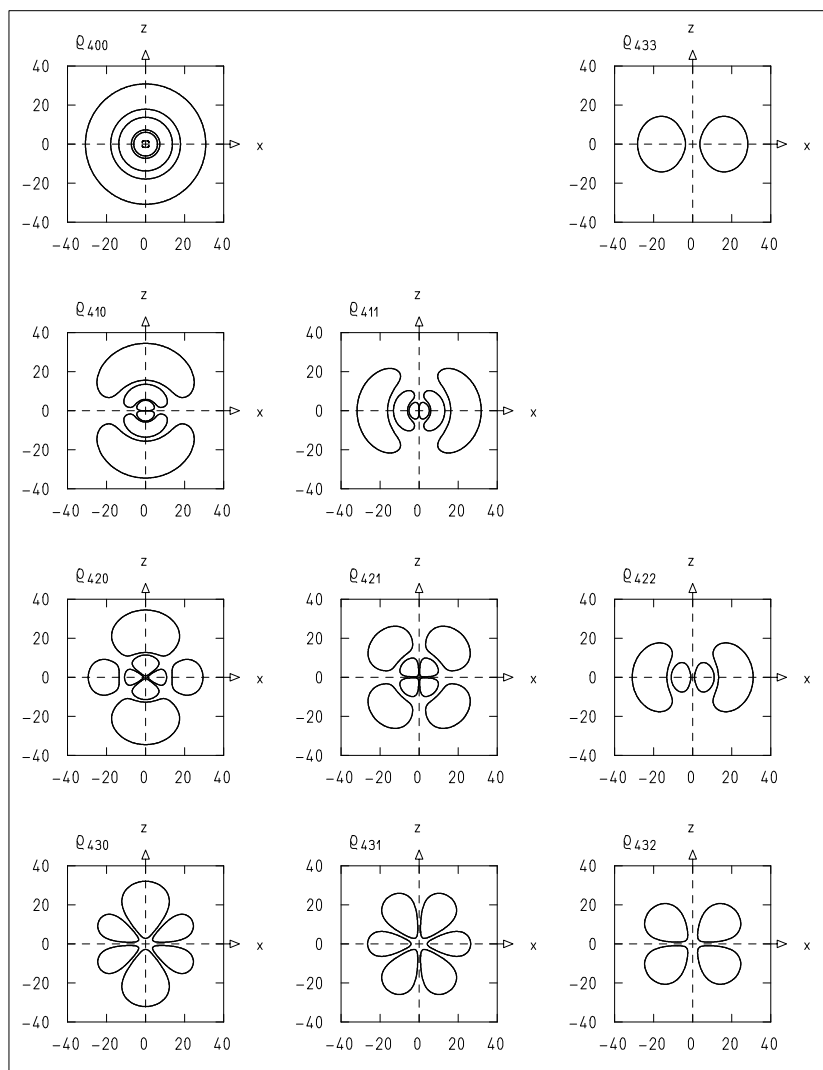


**Fig. 13.23.** Contour lines  $\rho_{4\ell m} = 0.00002$  in the  $x, z$  plane. Numbers are in units of the Bohr radius.

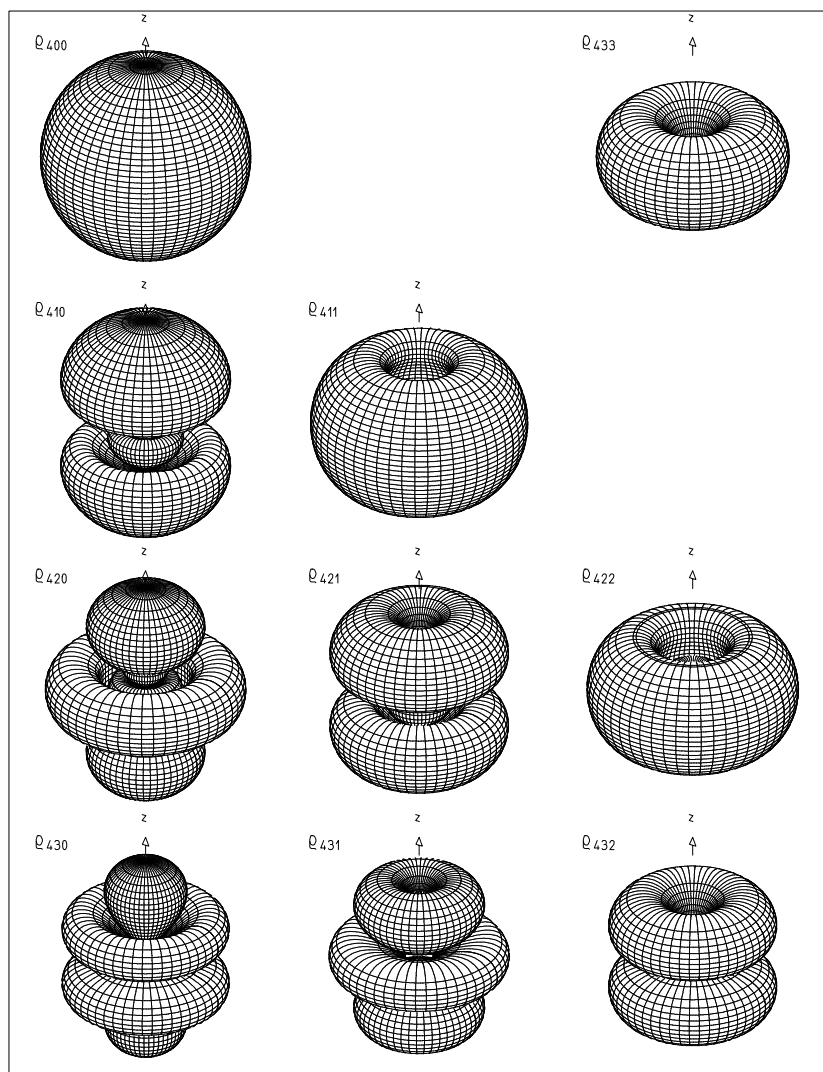


**Fig. 13.24.** Surfaces of constant probability density  $\rho_{4\ell m} = 0.00002$  in  $x, y, z$  space.

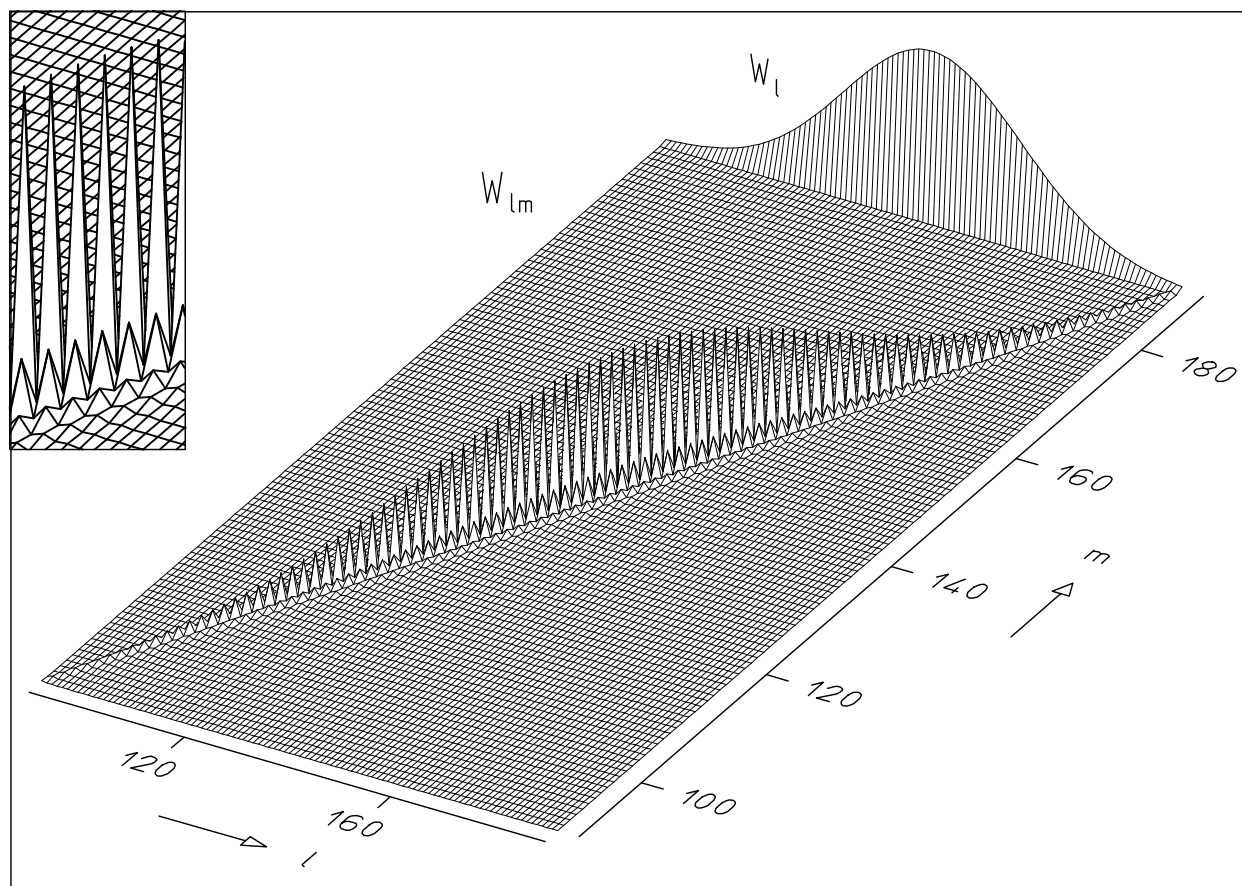
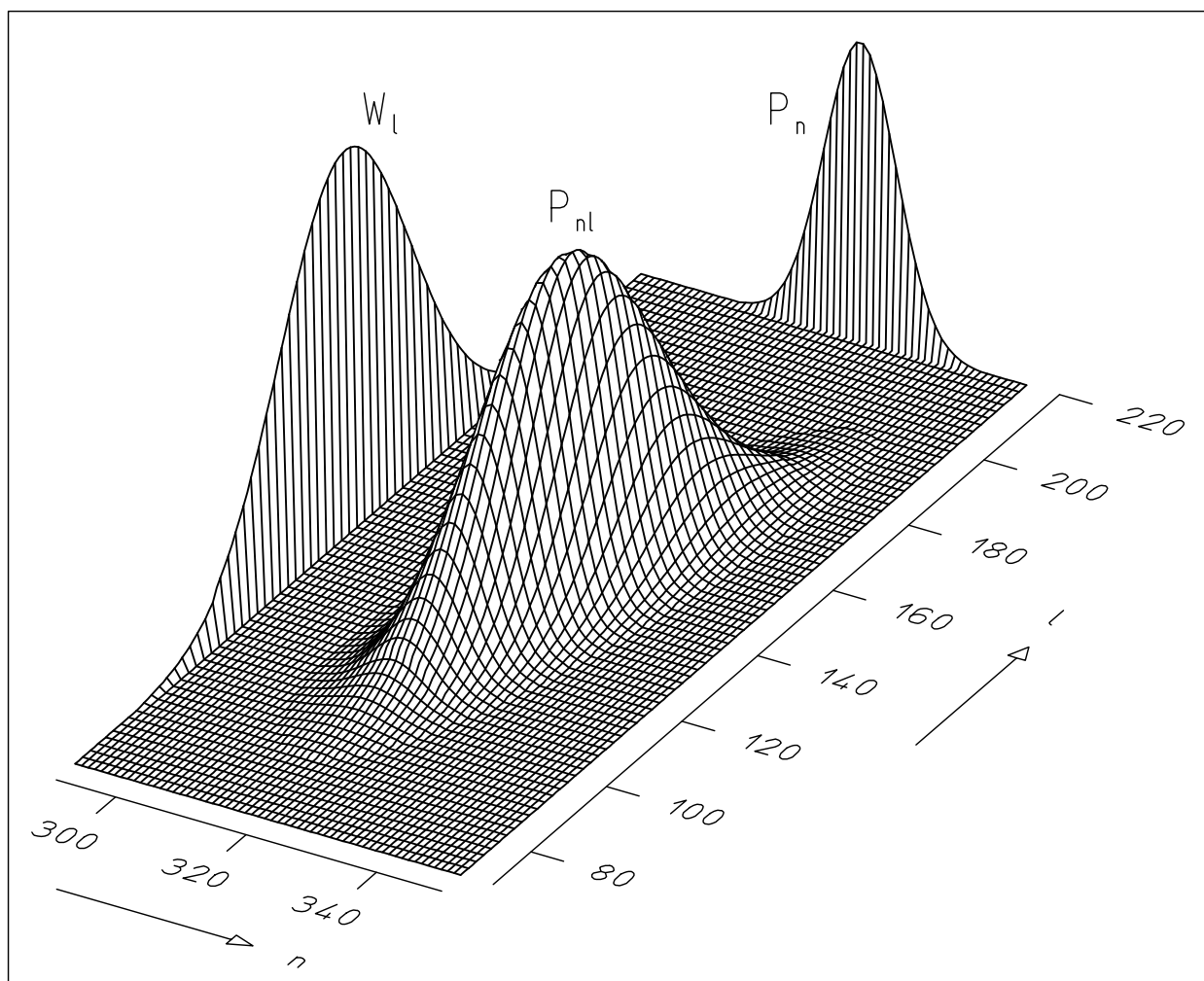
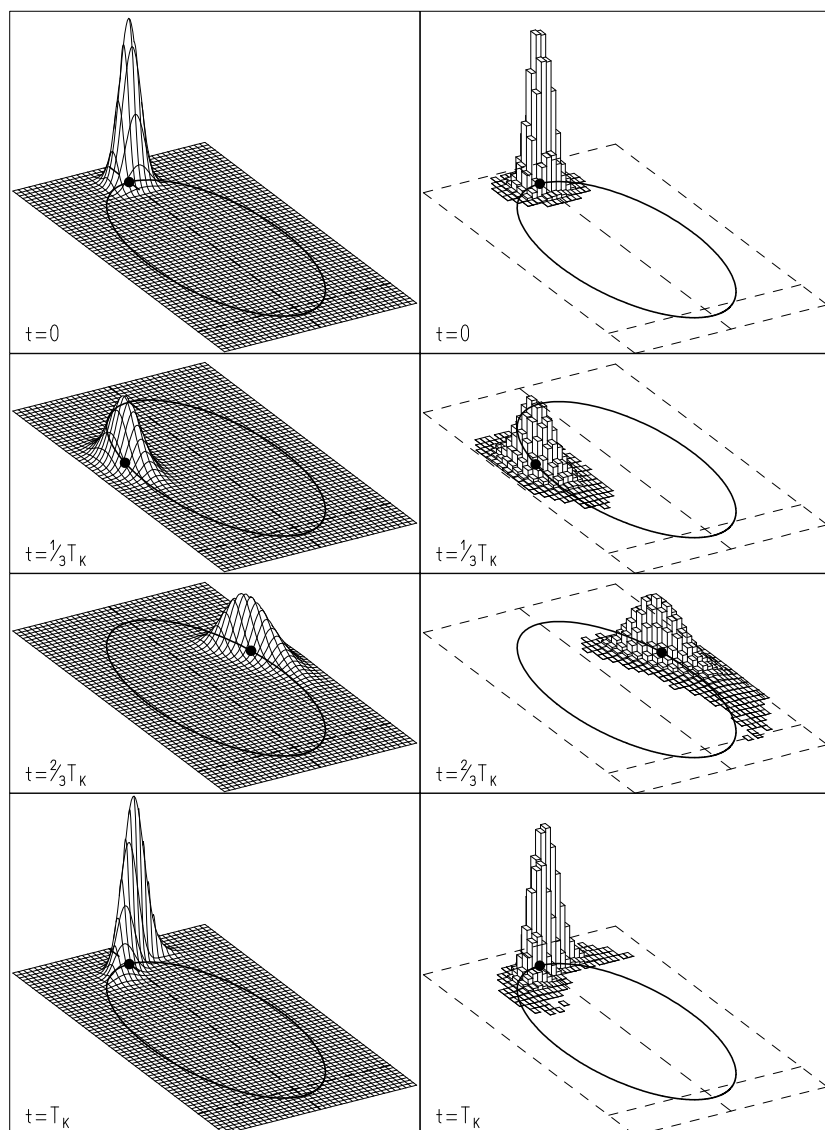


Fig. 13.25. Distributions of the probabilities  $W_{\ell m}$  of the quantum number of total angular momentum  $\ell$  and its  $z$  component  $m$  for the wave packet shown in Figures 13.27 through 13.30. The quantities are defined for integer values of  $\ell$ ,  $m$  only. Their graphical representations are connected by straight lines. Also shown is the marginal distribution  $W_{\ell}$ . The inlay is a magnification of the central part of the figure.



**Fig. 13.26.** Probability distribution  $P_{nl}$  of the principal quantum number  $n$  and the angular-momentum quantum number  $\ell$  of the wave packet shown in Figures 13.27 through 13.30 together with the marginal distributions  $W_\ell$  and  $P_n$ . The probability is set equal to zero if  $P_{nl} < 10^{-5}$ .



**Fig. 13.27.** Plots in the left column show the time evolution of an initially Gaussian wave packet in the plane  $z = 0$ , i.e., the plane of the classical Kepler orbit indicated by the ellipse. The full dot represents the corresponding position of the classical particle. The temporal instants shown are the thirds of the first Kepler period  $T_K$ . Plots in the right column show the time evolution of the spatial probability density of the corresponding classical phase-space distribution.

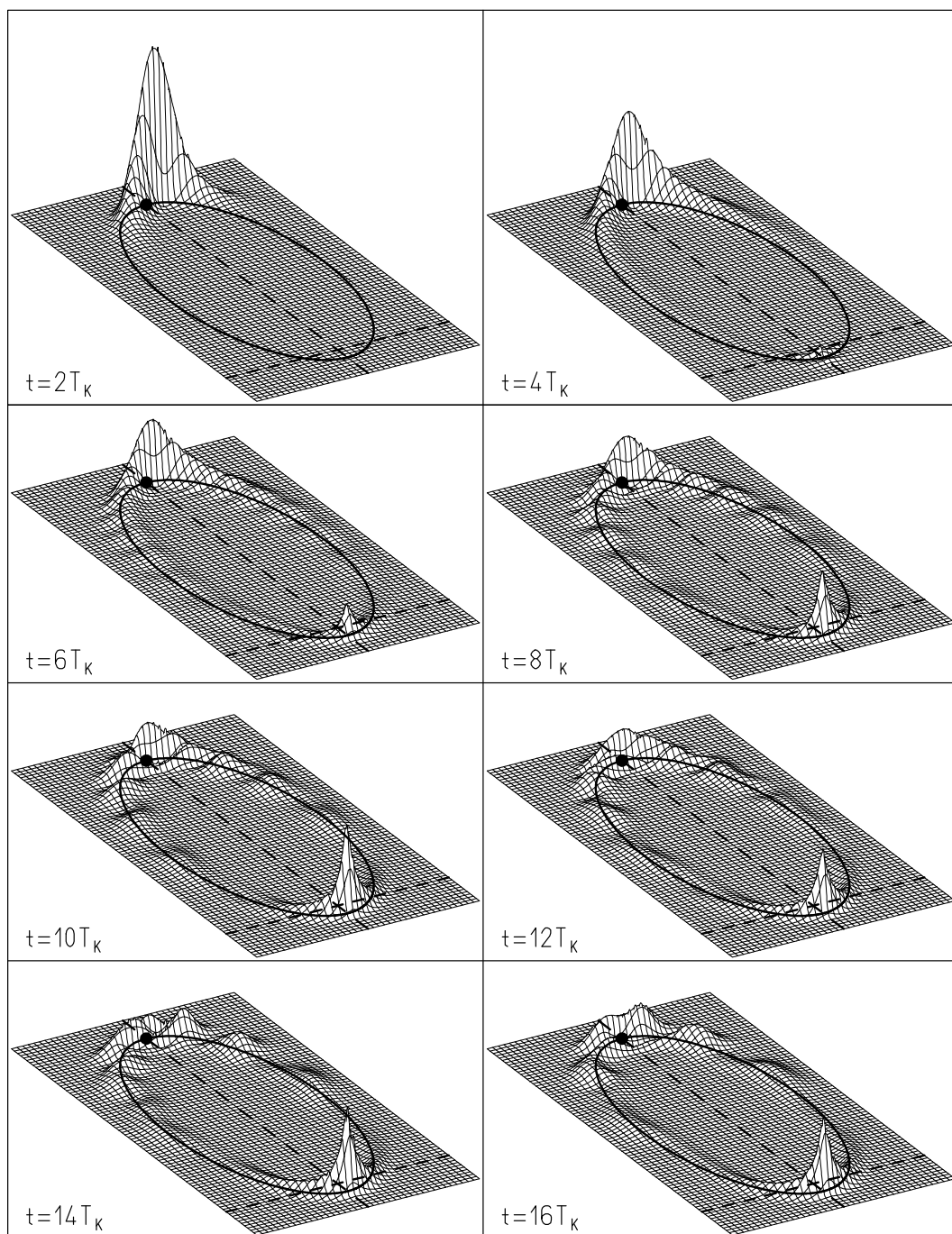


**Fig. 13.28.** Quantum-mechanical probability density in the Kepler plane for various multiples of the Kepler period. The wave packet widens from period to period. Once both ends of the wave packet overlap, interference sets in.



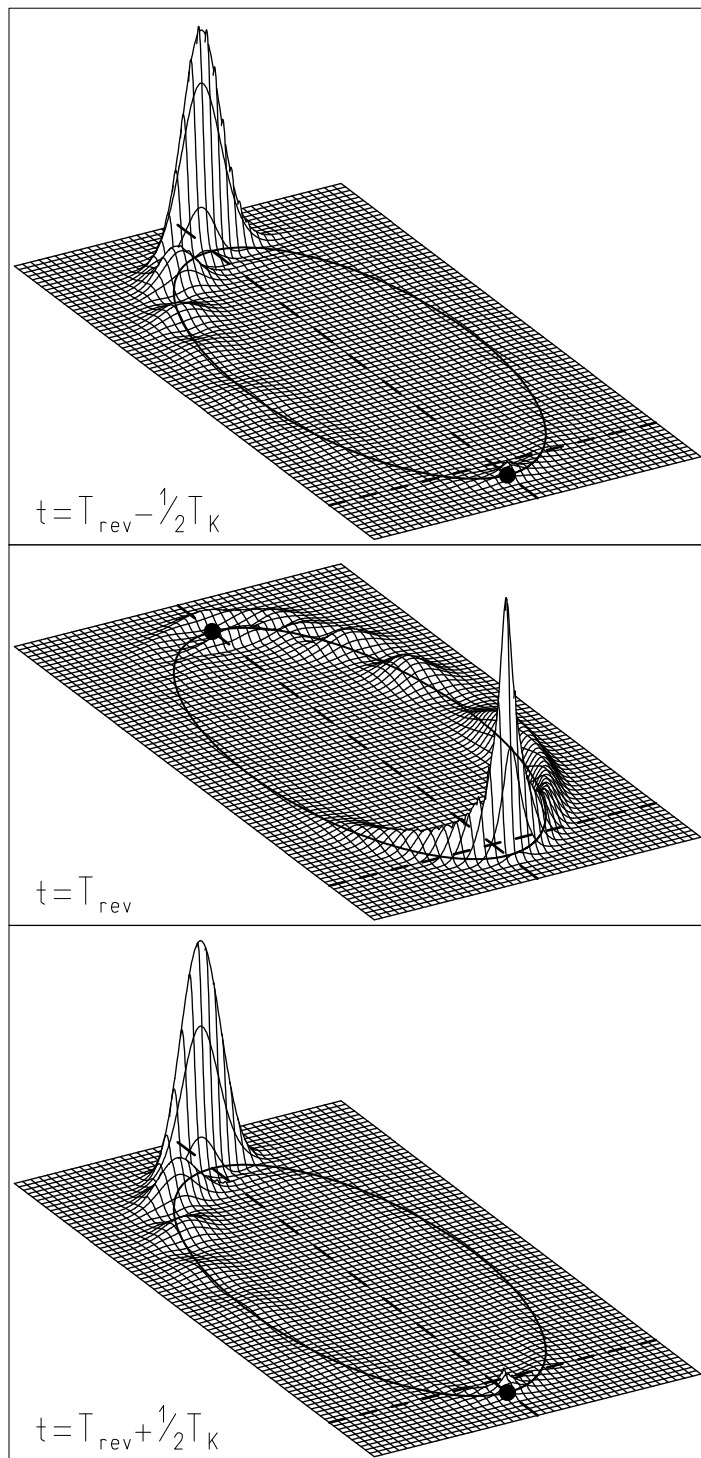


**Fig. 13.29** Revival of the wave packet for the times  $t = T_{\text{rev}} - T_K/2$ ,  $T_{\text{rev}}$ ,  $T_{\text{rev}} + T_K/2$ .

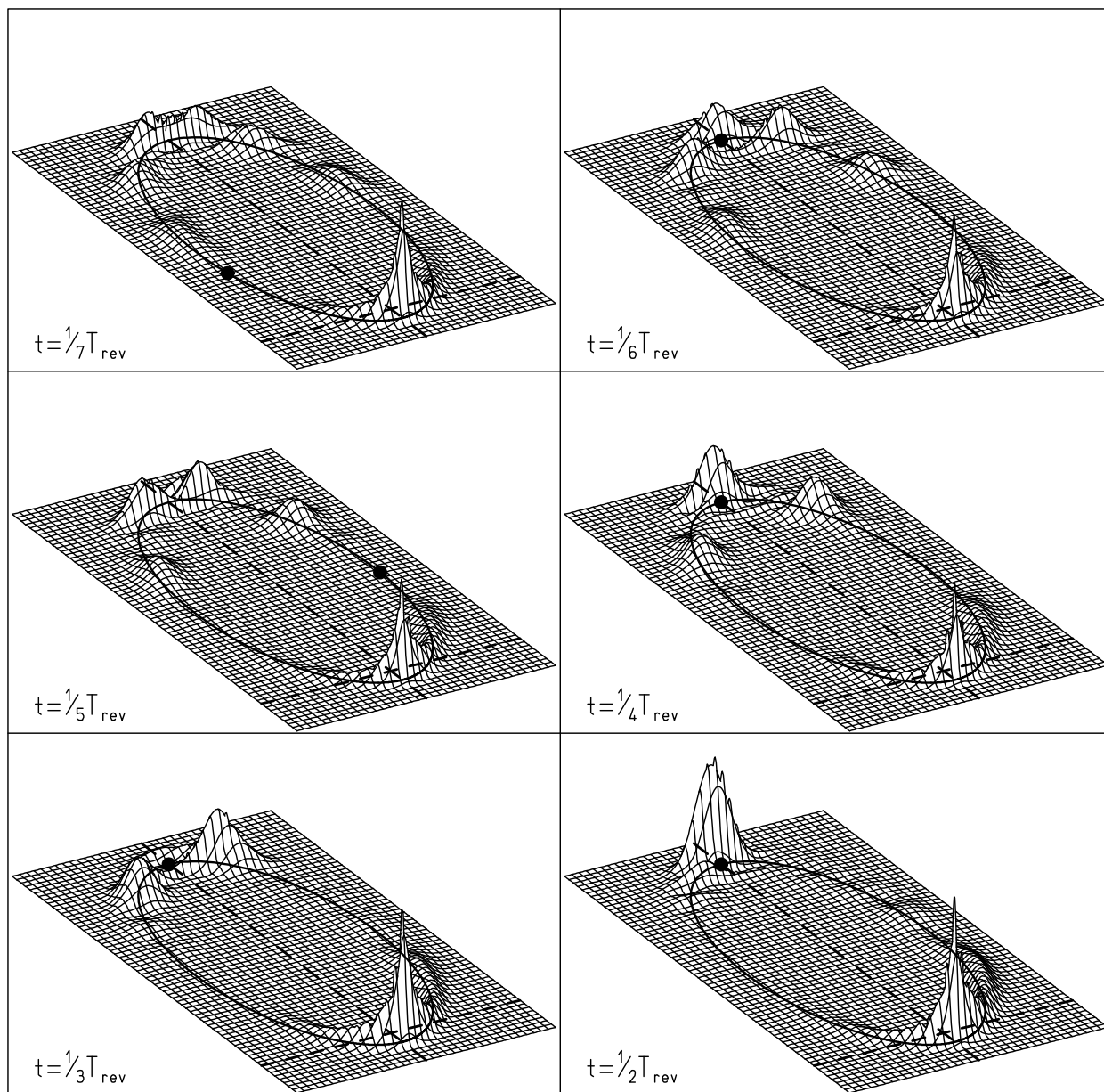


**Fig. 13.30.** Fractional revivals of the wave packet.